Article:
Javed, Z., Martinez, G.V., Mulero-Acevedo, M. et al. (2026) Improved MRSI in a murine glioma model using semiLASER: refining the metabolomics data obtained from murine models. Applied Sciences, 16 (8). 3788. ISSN: 2076-3417

https://doi.org/10.3390/app16083788

applied sciences

MDPI

Article

Improved MRSI in a Murine Glioma Model Using semiLASER: Refining the Metabolomics Data Obtained from Murine Models

Zoona Javed [1,2,†], Gary V. Martinez [3], Marta Mulero-Acevedo [1,4,5], Ana Paula Candiota [1,4,5], Carles Arus [1,4,5], Miquel E. Cabañas [2,4] and Silvia Lope-Piedrafita [2,4,6,*]

[1] Departament de Bioquímica i Biologia Molecular, Unitat de Bioquímica de Biociències, Edifici Cs, Universitat Autònoma de Barcelona, 08193 Cerdanyola del Vallès, Spain; z.javed@sheffield.ac.uk (Z.J.); marta.mulero@uab.cat (M.M.-A.); anapaula.candiota@uab.cat (A.P.C.); carles.arus@uab.cat (C.A.)
[2] Servei de Ressonància Magnètica Nuclear, Universitat Autònoma de Barcelona, Cerdanyola del Vallès, 08193 Barcelona, Spain; miquel.cabanas@uab.cat
[3] Department of Imaging Physics, The University of Texas M.D. Anderson Cancer Center, Houston, TX 77030, USA; gmartinez99@gmail.com
[4] Centro de Investigación Biomédica en Red en Bioingeniería, Biomateriales y Nanomedicina (CIBER-BBN), 08193 Cerdanyola del Vallès, Spain
[5] Institut de Biotecnologia i de Biomedicina (IBB), Universitat Autònoma de Barcelona, 08193 Cerdanyola del Vallès, Spain
[6] Departament de Bioquímica i Biologia Molecular, Unitat de Biofísica, Edifici M, Universitat Autònoma de Barcelona, 08193 Cerdanyola del Vallès, Spain
* Correspondence: silvia.lope@uab.cat
† Present address: School of Medicine and Population Health, The University of Sheffield, Sheffield S10 2TA, UK.

Abstract

Background: Magnetic resonance spectroscopic imaging (MRSI) offers valuable metabolic information for assessing brain tumor progression and therapeutic response, but its performance in rodent models is often hindered by the low signal-to-noise ratio (SNR) and spatially heterogeneous spectral quality, particularly in peripheral voxels. These issues reduce the number of usable spectra available for quantitative and classifier-based analyses. To address this, we implemented a multi-voxel MRSI-semiLASER sequence—widely recommended in clinical practice—on a 7T Bruker Biospec system running ParaVision 5.1 to improve spectral homogeneity in mouse brain tumor studies. Results: Compared with the vendor CSI-PRESS sequence, MRSI-semiLASER produced more uniform spectra across the grid and achieved up to a 1.2-fold SNR increase in murine glioma, enabling a 20% reduction in slice thickness without compromising spectral quality. Importantly, the sequence produced a substantial gain in the proportion of spectra amenable to analysis, particularly in outer grid voxels that frequently fail with CSI-PRESS. The implemented MRSI-semiLASER sequence and instructions are openly available to the community. Conclusions: MRSI-semiLASER improves spectral homogeneity, increases the proportion of usable spectra, and supports higher spatial detail. These technical improvements may enhance data yield per subject and may facilitate future applications such as more robust pattern recognition workflows and greater data efficiency in longitudinal studies, although such aspects were not evaluated here.

Keywords: spectroscopic imaging; brain tumor; semi-adiabatic LASER; chemical shift imaging; preclinical models

Academic Editors: Valeria Sacca and Fabiana Novellino

Received: 4 March 2026
Revised: 6 April 2026
Accepted: 8 April 2026
Published: 13 April 2026

1. Introduction

Magnetic resonance spectroscopy (MRS) and spectroscopic imaging (MRSI) provide unique metabolic information that complements conventional MRI [1–4]. ^{1}H MRS/MRSI have demonstrated added value in the diagnosis, classification, and treatment monitoring of brain tumors, including gliomas, by detecting biochemical alterations that often precede morphological changes [4–8]. Despite this potential, MRS and MRSI remain underutilized due to challenges in acquisition, processing, and interpretation [9,10].

Preclinical MRSI studies in animal models provide important advantages, even though they face additional technical challenges related to the small size of rodent brains—particularly in mice. These models enable highly controlled experimental conditions, repeated longitudinal measurements, and the possibility of direct histopathological validation even during transient response. Such approaches are not ethically feasible in human patients and strengthen the translational interpretation of metabolic findings for clinical studies [11–13]. Furthermore, immunocompetent mouse models, such as GL261 glioblastoma implanted in C57BL/6 mice, offer a biologically relevant environment in which to investigate tumor heterogeneity and therapeutic response [14–17].

Over the past years, our group has routinely applied ^{1}H-MRSI to study the GL261 glioma model and to develop pattern recognition-based classifiers for non-invasive assessment of therapy effects [6,18–21]. One of the main challenges in preclinical MRSI is achieving sufficient spatial detail to resolve the complex metabolic landscape of heterogeneous tumors. Insufficient spatial coverage can obscure important regional differences, which may hamper classifier performance. To broaden anatomical sampling, we implemented multi-slice MRSI acquisitions, allowing data collection across consecutive planes, and enhancing representation of glioma heterogeneity [18]. Nonetheless, our sustained experience has revealed a persistent technical limitation: the commercially available sequence, a chemical shift imaging sequence with point-resolved spectroscopy localization (CSI-PRESS), frequently provided heterogeneous spectral quality across the grid, with disproportionately poor SNR and degraded lineshapes near the edges of the excited volume. In practice, a non-trivial fraction of outer grid voxels became unusable for model training or classification, reducing effective sample size, biasing spatial coverage, and weakening downstream classifier generalization. A major contributor to this problem is the imperfect spatial excitation profile of the conventional refocusing pulses used in PRESS, as well as the chemical shift displacement errors (CSDEs) inherent to the sequence [22].

In response to these limitations, clinical MRS has increasingly favored semi-localized adiabatic selective refocusing (semiLASER) over PRESS. SemiLASER offers improved localization fidelity and greater robustness to B1 inhomogeneity. It frequently provides higher effective SNR by leveraging adiabatic refocusing pulses [22,23]. Importantly, the international MRS Consensus Group recommended the use of semiLASER over the more conventional PRESS sequence [23]. Because both PRESS and semiLASER are spin echo sequences, adopting semiLASER is a natural and workflow-compatible step. This may directly address the mechanisms responsible for outer grid spectral degradation, while maintaining continuity with the existing CSI-PRESS datasets that underpin our classifiers. However, it should be emphasized that confirming this statement will require future studies with larger cohorts and a systematic evaluation of classifier robustness. Such work will be essential to rigorously validate our hypothesis, as this cannot be achieved within the exploratory framework of the present study.

Yet, despite its demonstrated advantages in clinical systems, semiLASER remains underused in preclinical MRSI applications [24]. To improve spectral homogeneity and increase the proportion of analyzable voxels, which is particularly important for data-driven models, we implemented a multi-voxel MRSI-semiLASER sequence on a 7T Bruker

Biospec scanner running ParaVision 5.1. The performance of this sequence in mouse brain studies was validated. We hypothesized that its adiabatic refocusing pulses would produce more homogeneous spatial excitation and improved spectral quality across the grid, ultimately increasing the number of analyzable spectra as a potential enabler of improved classifier performance, which should be fully assessed and investigated in future work.

In this study, we describe the implementation, in vitro/in vivo validation, and performance of the MRSI-semiLASER. We compare it against the current standard CSI-PRESS protocol. Our aim was to establish a robust and reproducible preclinical MRSI approach that enhances data quality. Furthermore, we expect it to facilitate more accurate downstream analysis and to be better aligned with clinical practice at the methodological level, as semiLASER is the clinically recommended localization sequence, potentially increasing the translational value of metabolic imaging in glioma research. This study does not directly evaluate classifier performance or clinical translation.

2. Materials and Methods

2.1. Phantom Preparation

The implemented MRSI-semiLASER sequence was first validated in vitro using a phantom mimicking mouse brain/brain tumor metabolite concentration [25] made of a 15 mL cylindrical falcon tube containing 12.5 mM N-acetylaspartate (NAA), 10 mM creatine (Cr), and 5 mM lactate (Lac) in a phosphate-buffered saline solution. Sodium azide (NaN_3, 0.27 g/L, 4.1 mM) was added to prevent bacterial growth. The phantom solution's pH was maintained at 7.5.

2.2. Animal Preparation and Specific Housing Conditions

Six C57BL/six female mice weighing 20–23 g obtained from Charles River Laboratories (L'Arbresle, France) were used in this study. Three were used as wild-type (WT) control mice, and the other three were glioma-bearing mice, whose tumors were induced by intracranial stereotactic injection of 10^5 GL261 cells, as described in [11]. Analgesia with meloxicam (Boehringer Ingelheim, Ingelheim am Rhein, Germany) was administered at 24 and 48 h post-implantation. The mice were housed at the animal facility of the Universitat Autònoma de Barcelona (Servei d'Estabulari https://www.uab.cat/ca/servei-estabulari, accessed on 15 September 2025) in an enriched environment and were allowed a 3-week rest, as described in [26]. The husbandry conditions were as follows: light:dark cycles: 12:12 h (light from 8 am to 8 pm); the temperature was maintained at 20 °C (±2 °C); the humidity was kept at 55% Hr (±10%); water and food were available ad libitum (2014 Teklad Global 14% protein rodent maintenance diet; Harlan, Gannat, France); individually ventilated cages were limited to five animals maximum (Tecniplast, Buguggiate, Italy). The GL261 mouse glioma cells were obtained from the Tumor Bank Repository at the National Cancer Institute (Frederick, MD, USA). All animal studies were approved by the local ethics committee (Comitè d'Ètica en la Recerca CERec https://www.uab.cat/ca/etica-recerca accessed on 6 April 2026) according to the regional and state legislation, registry number CEEAH 3665.

Animal well-being and health status in tumor-bearing mice were monitored daily by qualified research and/or facility staff, following strict parameters outlined in the approved protocol. The experiment was halted immediately upon reaching the designated humane endpoint. A structured veterinary assessment protocol was implemented to evaluate humane endpoints, including: body weight measurement (mandatory euthanasia if weight loss exceeds 20%), overall fur condition, and the presence of wounds or any movement restrictions impairing access to food or water. A scoring system was applied based on the following criteria: the maximum score in any single category requires immediate

euthanasia, and a cumulative score exceeding 10 points also mandates euthanasia. No delay between animal inspection and euthanasia was permitted, and no tumor-bearing animal died prior to reaching the humane endpoint. Wild-type (WT) mice were euthanized at the conclusion of the experiments in compliance with regulations that prohibit maintaining animals beyond the approved protocol period. Euthanasia was performed by cervical dislocation. All researchers responsible for animal handling received official FELASA (Federation of European Laboratory Animal Science Associations)-recognized training provided by the Universitat Autònoma de Barcelona (UAB).

2.3. MRI/MRS Studies

All MR experiments were performed at the joint nuclear magnetic resonance facility of the Universitat Autònoma de Barcelona and Centro de Investigación Biomédica en Red—Bioingeniería, Biomateriales y Nanomedicina (CIBER-BBN) (Cerdanyola del Vallès, Spain), Unit 25 of NANBIOSIS (https://www.nanbiosis.es/portfolio/u25-nmr-biomedical-application-i/ accessed on 6 April 2026). The experiments were conducted on a 7T Bruker Biospec 70/30 USR preclinical scanner using ParaVision 5.1 (Bruker BioSpin GmbH, Ettlingen, Germany) equipped with a quadrature receive surface coil, actively decoupled from a volume resonator, with an inner diameter of 72 mm. The mice were placed in a bed with a restraint system including ear bars and a bite bar for fixation of the head. The mice received anesthesia with 1–1.5% isoflurane in O_2 at 1 L/min. Their breathing rates were constantly monitored with a pressure probe and kept between 60 and 80 breaths/min (SA Instruments, Inc., New York, NY, USA). Mouse body temperature was monitored using a rectal probe and maintained at 37 ± 1 °C with a heated recirculating water system incorporated in the animal bed. The overall acquisition length for in vivo experiments was 3.5 h, including MRI and MRSI. After the MRI/MRSI acquisition, the mice were allowed to fully recover in a warm environment under infrared-controlled light and constant supervision. Upon recovery, the mice were carefully checked and returned to the animal facility.

2.4. MRI Protocol

Anatomical low-resolution T2-weighted (T2w) images were initially acquired in axial, sagittal, and coronal planes, and they were used as reference images to position the MRSI grids. A rapid acquisition with relaxation enhancement (RARE) sequence was used: RARE factor = 8; repetition time (TR) = 4200 ms; effective echo time (TE_{eff}) = 36 ms; field of view (FOV) = 19.2 × 19.2 mm^2; matrix size (MTX) = 128 × 128 (150 × 150 mm/pixel); number of slices (NS) = 14; slice thickness (ST) = 1 mm; interslice thickness = 1.1 mm; number of averages (NA) = 1; and total acquisition time (TAT) = 24 s. A specific reference image matching MRSI slice location was acquired for each MRSI study with a RARE sequence: RARE factor = 8; TR/TE_{eff} = 3000/36 ms; FOV = 17.6 × 17.6 mm^2; MTX = 256 × 256; ST = 1 mm; NA = 3; TAT = 3 min 36 s.

2.5. MRSI 2D CSI-PRESS Protocol

The performance of the newly implemented MRSI-semiLASER sequence was compared to the commercially available CSI-PRESS sequence using our standard protocol, also described in previous studies [18,27]: TR = 2500 ms; TE = 14 ms; Hermite-shaped pulses (90° excitation: 0.6 ms/9000 Hz; 180° refocusing: 0.6 ms/5400 Hz) were applied using the automatic reference power calibration determined during the initial Localizer (Tripilot) scan.

2.6. Common MRSI Protocol Parameters

The common protocol parameters that were used were: FOV = 17.6 × 17.6 mm^2; ST = 1 mm; volume of interest (VOI) positioned approximately in the center of the brain/phantom = 6.6 × 6.6 × 1.0 mm^3 (5.5 × 5.5 × 1.0 mm^3 for the upper and lower grids in mouse brain multi-slice acquisitions to avoid the skull); spectral width = 4006.41 Hz (13.34 ppm); points in the time domain = 2048. k-space was sampled using the available weighted acquisition mode in ParaVision 5.1, which applies a Hanning window in k-space to suppress side lobes and improve the spatial response function [28], with NA of 512. Spatial resolution was defined by an 8 × 8 voxel matrix over the field of view (nominal resolution, 4.84 µL) reconstructed, after Fourier interpolation to a 32 × 32 matrix, thus resulting in a 12 × 12 inner-grid matrix within the VOI (or a 10 × 10 matrix for 5.5 × 5.5 mm^2 VOI used in the upper and lower grids in multi-slice acquisitions). Linear and second-order shims were automatically adjusted. Initially, FASTMAP [29] was used within a 5.8 × 5.8 × 5.8 mm^3 volume, avoiding brain edges, which partially contained the MRSI VOI. Afterwards, a PV5.1 PRESS method-specific shim adjustment was performed over the MRSI VOI, leading to final waterline full widths at half maximum (FWHM) values of 13–19 Hz inside the VOI. Water suppression was performed with VAPOR using a bandwidth of 300 Hz. Also, six saturation slices (slice thickness = 10 mm; sech-shaped pulses = 1.0 ms/20,250 Hz) were positioned around the VOI to minimize outer volume contamination in the obtained signals. The TAT was 21 min for each MRSI dataset.

2.7. MRSI-semiLASER Implementation

For the implementation of the MRSI-semiLASER sequence, the PRESS localization block was replaced by a semiLASER localization block (see Supporting Information (SI) Figure S1), essentially, as described in [30]. The semiLASER block was composed of a conventional slice-selective excitation using a frequency-selective Hermite pulse combined with a slice gradient (as in CSI-PRESS), followed by a pair of 180° adiabatic full passage (AFP) Hyperbolic secant (HS) pulses combined with slice-selective gradients for the slice-selective refocusing in the two remaining perpendicular directions (instead of the conventional Hermite refocusing pulses used in CSI-PRESS). The spin echo condition was maintained whenever $\tau_1 + \tau_3 + \tau_5 = \tau_2 + \tau_4$ [30], where t_i are the time delays, as defined in Figure S1. In this implementation, the condition $\tau_2 = \tau_3$ was maintained for all values of TE, hence the spin echo condition was satisfied when $\tau_5 = \tau_4 - \tau_1$. A pair of crusher gradients along x, y, and z directions were also positioned symmetrically around each AFP pulse to suppress spurious signals (not depicted in the pulse sequence diagram for clarity). The 180° refocusing adiabatic pulses were generated using the TopSpin 2.0 PV stdisp tool. The implemented MRSI-semiLASER pulse sequence, along with the corresponding implementation instructions, has been made openly accessible through the Zenodo repository. For the MRSI-semiLASER sequence, the excitation pulse was kept the same as in CSI-PRESS (90° Hermite pulse 0.6 ms/9000 Hz), while the 180° refocusing pulses consisted of 2 ms/9 kHz HS adiabatic pulses. The MRSI-semiLASER experiments were conducted using a TE value of 27 ms, which was the minimum TE achieved with this sequence implementation. All other acquisition parameters were common to the CSI-PRESS protocol.

2.8. Data Processing and Analysis

The MRSI acquired datasets were pre-processed at the MR workstation with ParaVision 5.1 (Bruker BioSpin GmbH, Ettlingen, Germany) using the csi_dash macro by applying an exponential multiplication, resulting in a 4 Hz line broadening, zero- and first-order phase correction, and in-plane interpolation to 32 × 32. The 3D Interactive Chemical Shift Imaging (3DiCSI) software, package version 1.9.17 (Courtesy of Truman Brown, Ph.D., Columbia University, New York, NY, USA), was used for data visualization.

For sequence performance comparisons, the SNR and FWHM were computed, using in-house-developed MATLAB R2019b scripts [31] since they are the most relevant factors affecting spectrum classification [32–34] in our pattern recognition studies. The SNR was calculated for each individual spectrum as the height ratio of the metabolite peak to the standard deviation of the noise (noise range taken from −1 to 0 ppm). FWHM was calculated by fitting the metabolite peak to a Lorentzian lineshape using the op_getLW function from the FID-A pipeline [35].

Spectral quality was evaluated visually by two independent spectroscopists who were blinded to the acquisition sequence. The spectra were classified as of unsuitable quality when presenting one or more of the following features: (i) the absence of clearly distinguishable metabolite peaks at their expected chemical shift positions, (ii) marked baseline distortion, and (iii) evident artefactual signals.

2.9. Repeatability and Reproducibility Tests

To evaluate the reliability of the implemented MRSI-semiLASER sequence, repeatability and reproducibility tests were first performed in the phantom and compared to CSI-PRESS. Repeatability, understood as the degree to which the same measurement can be obtained under identical conditions over a short period, was assessed by running what we refer to as "intraday" experiments. For that, three consecutive datasets were acquired by cloning the previous scan without altering any parameters or adjustments. Reproducibility, understood as the degree to which the same measurement can be obtained under changed conditions, such as time, sample positioning, or shimming adjustments, was assessed by running what we refer to as "interday" experiments. For this, the MRSI data sets were acquired on three separate days using the same phantom and acquisition settings. However, slight differences may occur in other adjustment parameters, such as phantom positioning, shimming, frequency, pulse power, or receiver gain automatic adjustments. From these experiments, the coefficient of variation (CoV), defined as the ratio of the standard deviation (SD) to the mean, and the repeatability coefficient (RC) [36] were estimated.

2.10. Statistics

Pairwise comparisons between sequences (CSI-PRESS vs. semiLASER) were performed using a two-tailed paired *t*-test applied to per-subject (in vivo) or per-experiment (phantom) values. To control for multiple testing, the false discovery rate (FDR) correction was applied within predefined families of comparisons (phantom, WT, and tumor), using an adjusted significance threshold of p_FDR < 0.10, appropriate for exploratory analyses with limited sample size. Given the small sample size per group ($n = 3$), effect sizes were computed using Cohen's dz (dz values of ~0.2, 0.5, and 0.8 denote small, medium, and large effects, respectively, and dz > 1 represents a very large within-subject effect). The unit of analysis was the animal (in vivo) or the independent phantom acquisition (in vitro), avoiding voxel-level pseudoreplication. Statistical significance was defined at $p \leq 0.05$ (uncorrected) and, where applicable, after multiple testing correction using the FDR-adjusted criterion (p_FDR ≤ 0.10).

3. Results

3.1. Performance of the Implemented MRSI-semiLASER Sequence In Vitro

The implemented MRSI-semiLASER sequence was initially compared to the commercially available CSI-PRESS sequence in vitro. A phantom containing NAA and Cr at physiological concentrations in the WT mouse brain and Lac at a concentration comparable to that measured in mouse brain glioma [25,37],was used for this purpose. The best-

performing MRSI-semiLASER protocol had a minimum TE of 27 ms for the implemented MRSI-semiLASER sequence. It was compared with the PRESS-CSI protocol that we used in our previous studies [18,20], with a TE of 14 ms. Identical values were used for TR, FOV, MTX size, SW, shimming, and all other acquisition parameters, as described in the methods section. Figure 1 shows the MRSI datasets using the implemented MRSI-semiLASER sequence (top) and CSI-PRESS (bottom) in the phantom. The corresponding SNR maps for NAA (signal at ca. 2 ppm), overlaid on the phantom T2w image, are shown in the central panel, demonstrating higher SNR values for the MRSI-semiLASER sequence. Moreover, the MRSI-semiLASER NAA maps showed a visually more homogeneous appearance compared to the CSI-PRESS maps. Representative individual spectra from the central and bottom-right 4 × 4 sub-grids are shown on the left and right panels, respectively (see spectrum signal assignments in Figure S2). In the central sub-grid, similar spectral profiles to those obtained with CSI-PRESS were observed for the MRSI-semiLASER sequence, but with higher signal intensities/SNR. More significant disparities between the two sequences were noted at the periphery of the MRSI grid.

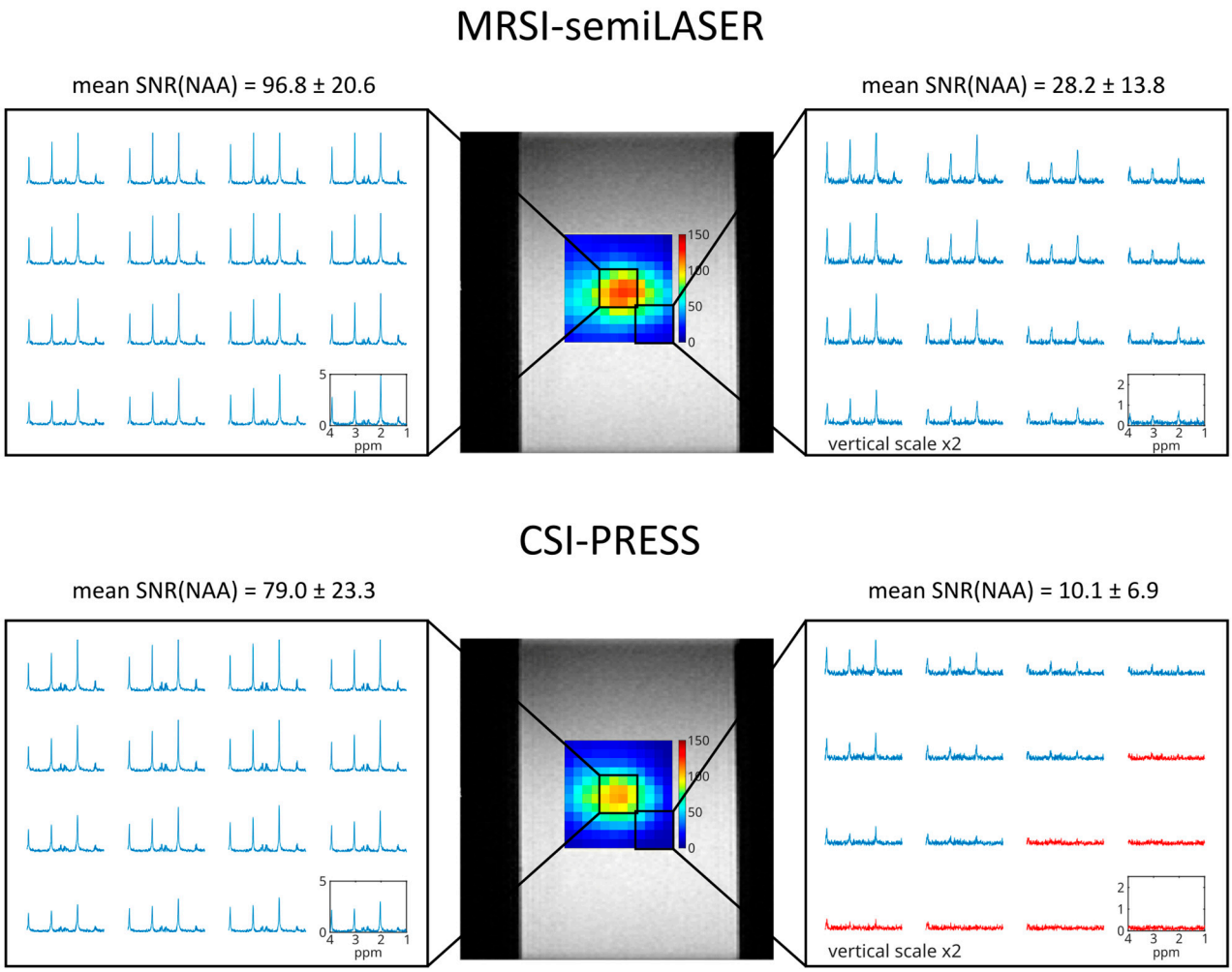

Figure 1. Representative phantom MRSI results. MRSI-semiLASER (**top**) vs. CSI-PRESS (**bottom**). Corresponding SNR maps for NAA at ca. 2 ppm (using same scale), overlaid on the phantom T2w images (**middle panels**). Individual spectra from the 4 × 4 sub-grid from the center (**left**) and from the bottom-right grid (**right**). Unsuitable quality spectra are shown in red.

As seen in the bottom-right sub-grid spectra, signal intensities were reduced compared to the central sub-grid in both sequences; nonetheless, well-defined resonances

were still detected in MRSI-semiLASER, whereas in CSI-PRESS spectra, many of the resonances vanished within the noise level (see red spectra). In vitro MRSI-semiLASER showed 26% mean SNR increase for the central 4 × 4 sub-grid and 155% for the bottom-right 4 × 4 sub-grid, with respect to CSI-PRESS (see Table S1). The large increase in the semiLASER SNR in the outer sub-grid can be attributed to the better excitation profile of the adiabatic refocusing pulses compared to the Hermite pulses used in CSI-PRESS. The semiLASER sequence was also less influenced by the chemical shift displacement error (CSDE), which is expressed as a percentage of the voxel size and is given by the ratio of the chemical shift difference (in Hz) between the two resonances of interest and the bandwidth of the frequency-selective pulse [23]. For CSI-PRESS, the CSDE between water signal at 4.7 ppm and Lac at 1.3 ppm (chemical shift difference of 3.4 ppm) in x, y, and z directions was 14.2%, 14.2%, and 9%, respectively, whereas the CSDE was reduced in the x and y directions to 8.9% with MRSI-semiLASER. In z direction, the CSDE was the same in both sequences since they used the same Hermite 90° excitation pulse.

To evaluate the reliability of the implemented MRSI-semiLASER sequence, repeatability and reproducibility tests were first performed in vitro, and they were compared to CSI-PRESS. In the "intraday" experiments, for repeatability evaluation, we ran three consecutive datasets by cloning the previous scan without altering any parameters or adjustments. In the "interday" experiments, for reproducibility evaluation, we obtained MRSI data sets on 3 separate days using the same phantom and acquisition settings. However, slight differences may occur in other adjustment parameters, such as phantom positioning, shimming, frequency, pulse power, or receiver gain. Mean spectra looked reproducible in intraday and interday experiments for both MRSI-semiLASER and CSI-PRESS (see Figure S2). Boxplots of the SNR values for NAA of all the spectra within the VOI are shown in the upper row of Figure 2 for interday experiments. A consistent pattern was observed for all acquisitions, with MRSI-semiLASER sequence having superior SNR compared to CSI-PRESS, which resulted in a boxplot with higher mean and limits for MRSI-semiLASER. These differences were also appreciated when comparing NAA SNR histograms shown in the bottom row in Figure 2. As can be seen, MRSI-semiLASER showed two to three spectra with the SNR values below 20, whereas in CSI-PRESS, close to 20 spectra had the SNR below 20 in all the acquisitions. Relevant differences were also detected in the upper SNR range, where distinctly fewer spectra with the SNR values above 80 in CSI-PRESS were found, as compared to MRSI-semiLASER. Similar results were observed in intraday experiments (see Figure S3). Both MRSI-semiLASER and CSI-PRESS showed reproducibility based on the SNR, although lower coefficients of variation and lower repeatability constants were tabulated for MRSI-semiLASER, indicating better reproducibility, as compared to CSI-PRESS (see Table S2). These differences were systematically observed in both intraday and interday experiments. As expected, higher CoV and RC values were also obtained for interday experiments as compared to intraday experiments due to the additional changing conditions affecting interday experiments. A significant increase in the SNR was observed for NAA in intraday experiments (29%) and for Cr in both intraday and interday experiments (22% and 21%, respectively). For NAA in the interday experiments, the 21% increase showed a trend toward significance (uncorrected $p = 0.08$; p_FDR = 0.10). No significant differences were found for Lac (see Figure S4 and Table S2).

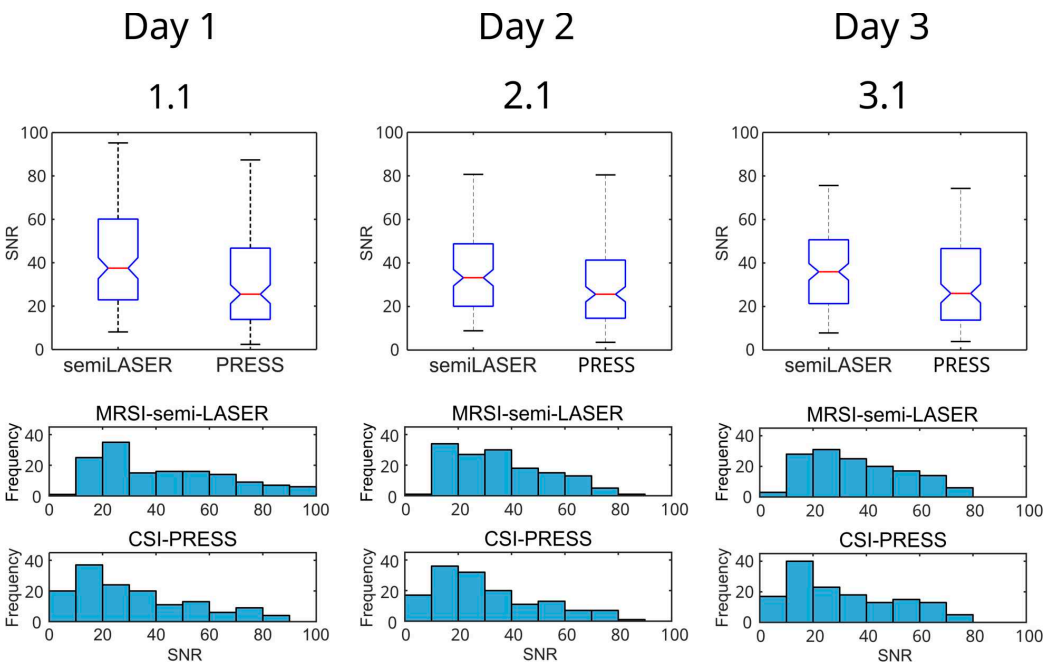

Figure 2. In vitro reproducibility study. NAA SNR boxplots (**top**) and frequency histograms (**bottom**) for interday experiments (DAY 1, DAY 2, and DAY 3) using MRSI-semiLASER and CSI-PRESS in a cylindrical phantom.

3.2. In Vivo Performance of the Implemented MRSI-semiLASER Sequence

After obtaining satisfactory results in vitro, the implemented sequence was further evaluated in WT mouse brain studies. Figure 3 shows representative datasets using the implemented MRSI-semiLASER sequence (top row) and CSI-PRESS (bottom row) from a C57BL/6 WT mouse brain, where the spatial heterogeneity and signal intensity can be visually compared. As found in the phantom studies, an overall signal increase in MRSI-semiLASER was notably evidenced by inspection of NAA SNR maps. The visual comparison of the MRSI spectra in the sub-sections was consistent with the phantom results, where differences were mainly observed between spectra within the outer MRSI grid. Well-resolved signals were obtained from voxels within the central grid (Figure 3, left), while noisier spectra were found in the outer sub-grids (Figure 3, right). Outer grid spectra acquired with the MRSI-semiLASER sequence visually appeared more homogeneous and with better spectral profiles as compared to the same located spectra from CSI-PRESS. CSI-PRESS outer grid had remarkably more voxels with signals within the noise level as compared to MRSI-semiLASER (see red spectra). In vivo MRSI-semiLASER showed a statistically significant 19% mean NAA SNR increase for the central 4 × 4 sub-grid and a notable 56% increase for the bottom-right 4 × 4 sub-grid, with respect to CSI-PRESS (SI, Table S3). A visual evaluation of the number of voxels with bad-quality spectra was assessed independently by two spectroscopist experts with ca. 86% inter-observer agreement. Although there was a suitable agreement between expert observations, authors acknowledge an absence of a formal inter-observer agreement metric, which should be implemented in future work. The proportion of unusable outer grid spectra decreased from approximately 18% with CSI-PRESS to 8% with MRSI-semiLASER, yielding a ~12% absolute increase in usable spectra across the grids, a gain that should directly benefit downstream classifier training and evaluation.

In vivo reproducibility studies were also performed by acquiring datasets using the same acquisition parameters in three WT mice (the mean spectra are shown in Figure S5). The mean SNRs within the entire 12 × 12 grid were computed and averaged for the three studies, for NAA, Cr, and Cho peaks. MRSI-semiLASER showed a mean increase of 15%

for NAA, 5% for Cr, and 8% for Cho, being only significantly different for NAA (Figure S6). Slightly lower variations were obtained for semiLASER compared to CSI-PRESS (Figure S5 and Table S4).

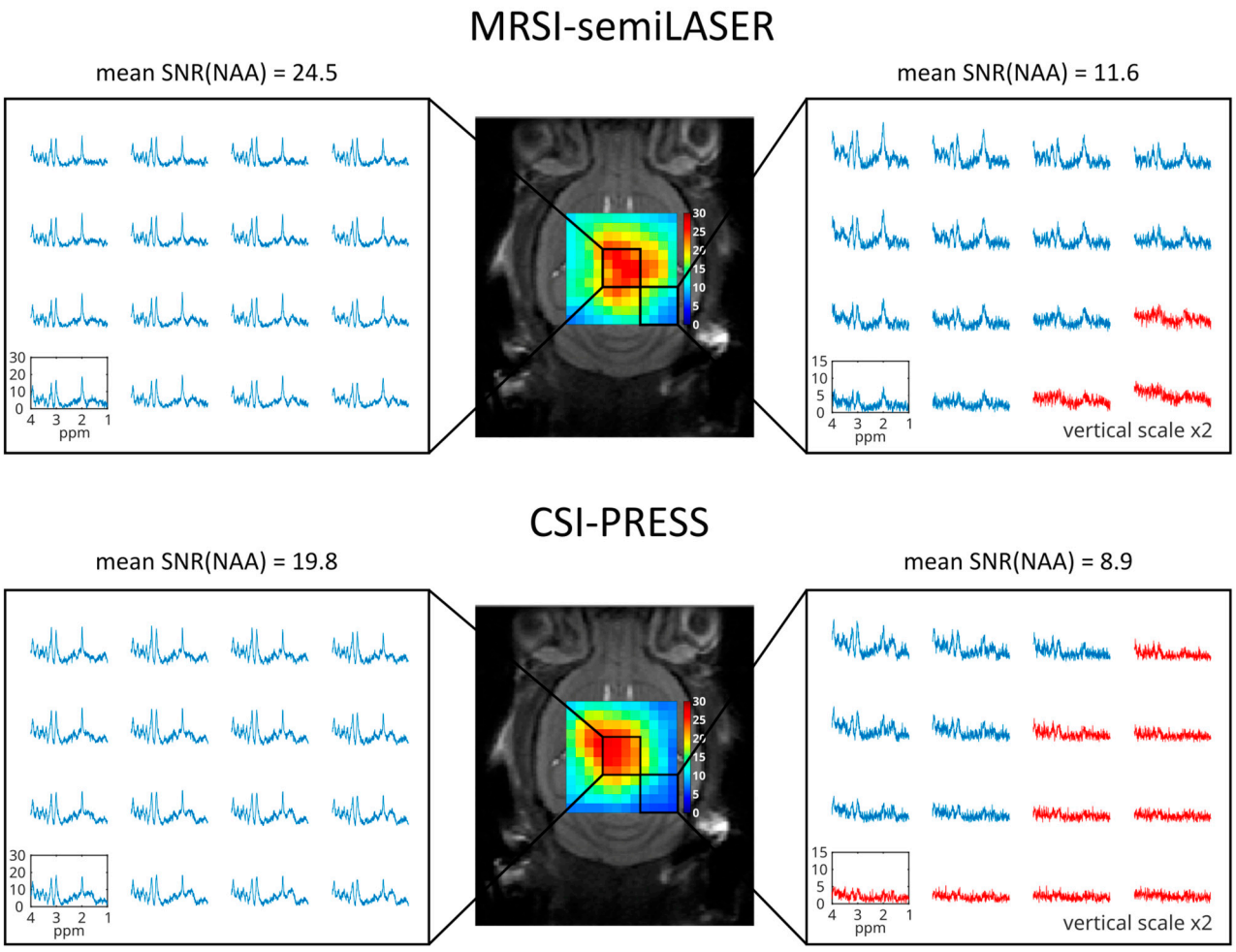

Figure 3. Representative WT mouse brain MRSI results. MRSI-semiLASER (**top**) vs. CSI-PRESS (**bottom**). Corresponding SNR maps for NAA (using same scale), overlaid on the mouse T2w images (**middle panels**). Individual spectra from the 4 × 4 sub-grid from the center (**left**) and from the bottom-right grid (**right**). Unsuitable quality spectra are shown in red.

MRSI-semiLASER was also evaluated in a murine model of GL261 glioblastoma and compared to CSI-PRESS. In Figure 4, representative mean spectra and standard deviation from GL261 tumor-bearing mouse brain datasets acquired with the implemented MRSI-semiLASER sequence and CSI-PRESS are displayed on the top panel, showing visually similar spectral profiles. The MRSI-semiLASER SNR map for lactate/mobile lipid/macromolecules (Lac/ML/MM) peak at 1.3 ppm, shown overlaid on the reference T2w image, appeared more homogeneous within the tumor region as compared to CSI-PRESS Lac/ML/MM SNR map (Figure 4, bottom). The mean SNR recorded for the Lac/ML/MM peak in the MRSI-semiLASER was 15.5 ± 1.0 versus 14.3 ± 1.6 in the CSI-PRESS sequence (Table S5). MRSI-semiLASER produced up to a 1.2-fold increase in the SNR as compared to the CSI-PRESS sequence for the Lac/ML/MM peak in tumor mouse brain, with a 1.1-fold mean increase value.

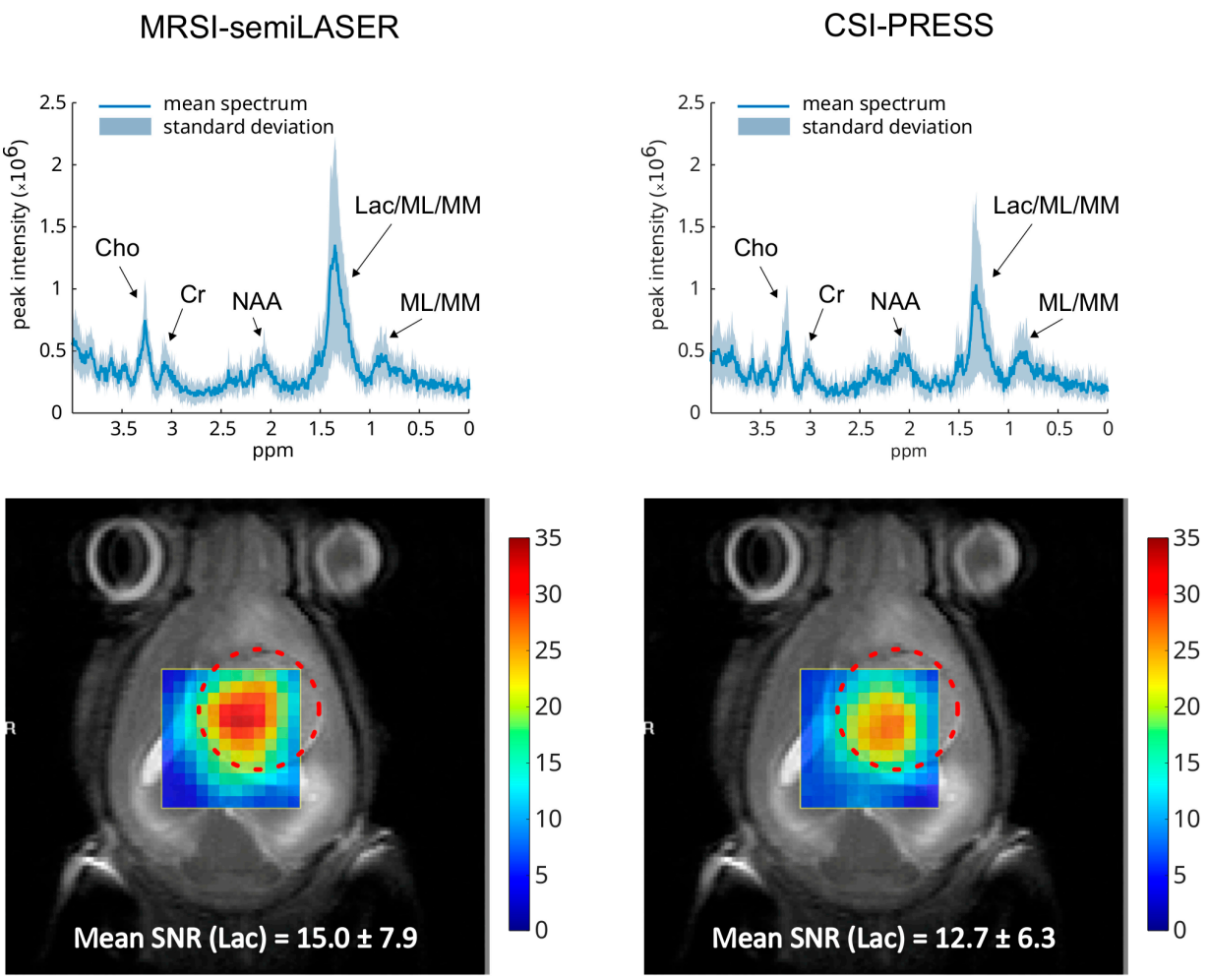

Figure 4. Representative MRSI data from a GL261 tumor-bearing mouse. Data acquired with MRSI-semiLASER (**left**) and CSI-PRESS (**right**). Mean spectra, depicted in blue, standard deviation in gray shades (**top**) with the corresponding assignments, and Lac/ML/MM SNR maps overlaid on the corresponding T2w images (**bottom**). The red circles indicate the approximate tumor abnormal zone detected in T2w MRI. The increase in the SNR indicates more effecting refocusing of the adiabatic pulses of the semiLASER sequence consequently contributing to its superior SNR performance.

3.3. Increased Slice-Direction Spatial Resolution Using MRSI-semiLASER Sequence In Vivo

Building on the increased SNR provided by the MRSI-semiLASER sequence, we evaluated whether reducing slice thickness could further improve the spatial detail of multi-slice 2D MRSI acquisitions. We therefore compared semiLASER datasets acquired at 0.8 mm slice thickness with those acquired at 1 mm, the value used in our routine CSI-PRESS protocol.

Representative spectra from peritumoral parenchyma and tumor regions for 0.8 mm and 1 mm slices are shown in Figure 5. Reducing slice thickness from 1 mm to 0.8 mm improved spectral definition, yielding narrower and more intense peaks in both regions. In the peritumoral parenchyma, the Lac/ML/MM resonance showed a FWHM decrease from 25.4 Hz (1 mm) to 21.5 Hz (0.8 mm), corresponding to a 15% reduction. Within the tumor region, the Lac/ML/MM FWHM decreased by 7%. Choline also exhibited improved linewidths, with a 9.3% reduction (23.5 Hz at 1 mm vs. 21.5 Hz at 0.8 mm) consistently observed in both tumor and peritumoral tissue.

Mean SNR values for Lac, NAA, Cr, and Cho across the full grid are summarized in Table S6. As expected from the 20% reduction in slice volume, the SNR values were lower at 0.8 mm. However, the observed SNR losses were modest: the maximum reduction was

11.5% for Cho and only 3.2% for Cr, both clearly below the ~20% decrease predicted by volume reduction alone. Thus, the 0.8 mm acquisition preserved the SNR more efficiently than expected while providing improved spectral sharpness and spatial detail.

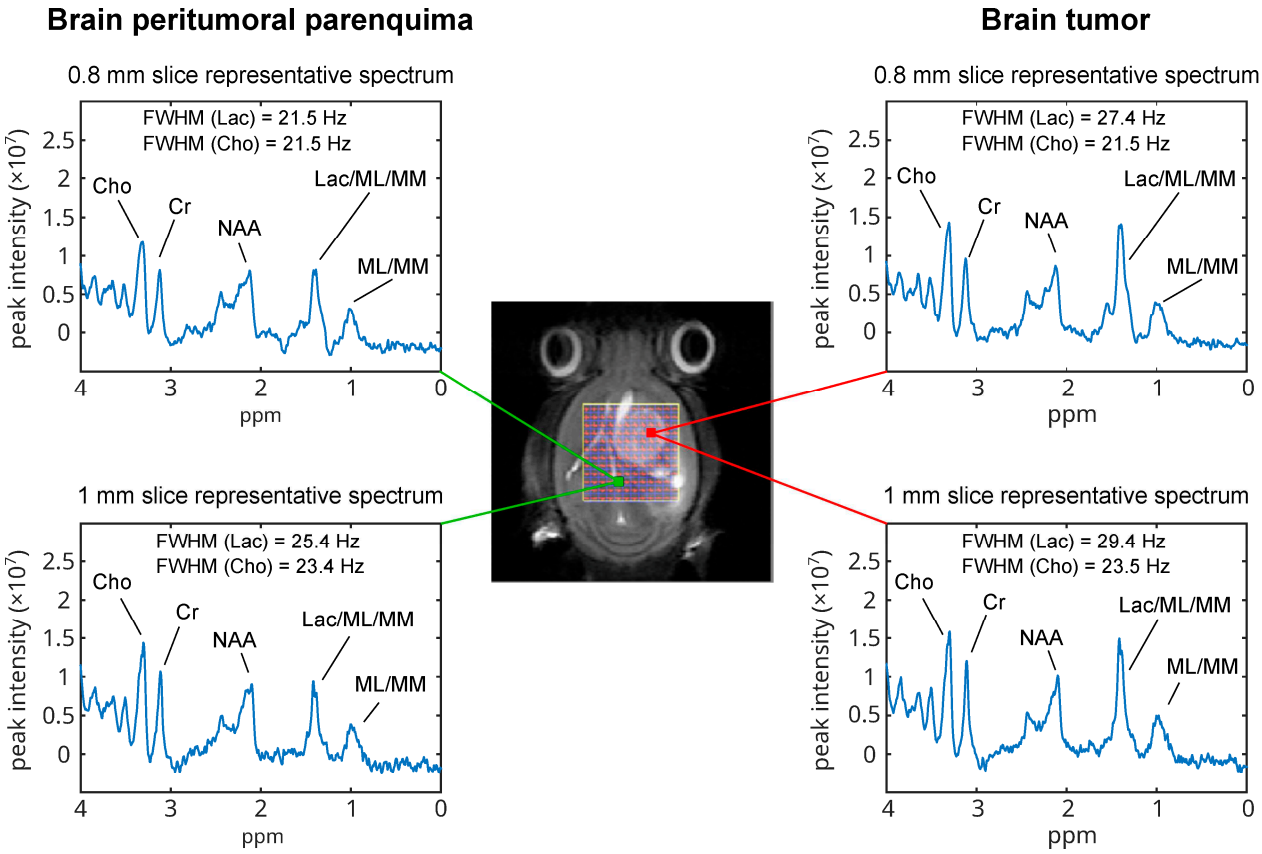

Figure 5. Comparison of 0.8 mm versus 1 mm slice thickness MRSI-semiLASER acquisitions. Representative spectra from brain peritumoral parenchyma (**left**) and tumor regions (**right**). Representative spectra from peritumoral parenchyma and tumor regions are indicated in green and in red, respectively, on the T2w image (**middle panel**). FWHM stands for full width at half maximum.

These promising results allowed us to satisfactorily acquire five consecutive 0.8 mm slice thickness grids across the tumor in GL261 tumor-bearing mice (Figure 6). These five slices encompassed the same volume as the four 1 mm slices obtained using the previous protocol, significantly improving the spatial resolution along the slice direction. T2w images were used as reference to locate the MRSI grids across the mouse brain, partially covering the tumor (Figure 6-left and middle). The VOI for the top and bottom slices was reduced to avoid contact with the skull. Consequently, the VOI dimensions were set to 6.6 × 6.6 × 1 mm^3 for the middle slices and reduced to 5.5 × 5.5 × 1 mm^3 for the top and bottom slices. Multi-slice MRSI grids were acquired sequentially, and shimming was performed individually for each MRSI grid. Lac/ML/MM intensity maps for each slice, overlaid on the corresponding T2w reference images, are shown on Figure 6 (right), demostrating increased signal intensity within the tumor region. Importantly, in addition to the improved spectral definition, the 0.8 mm multi-slice MRSI-semiLASER protocol also increased the total number of acquired spectra within the same anatomical volume (632 vs. 488 with the 1 mm CSI-PRESS protocol; see Table S7), further enhancing the overall data yield of the acquisition.

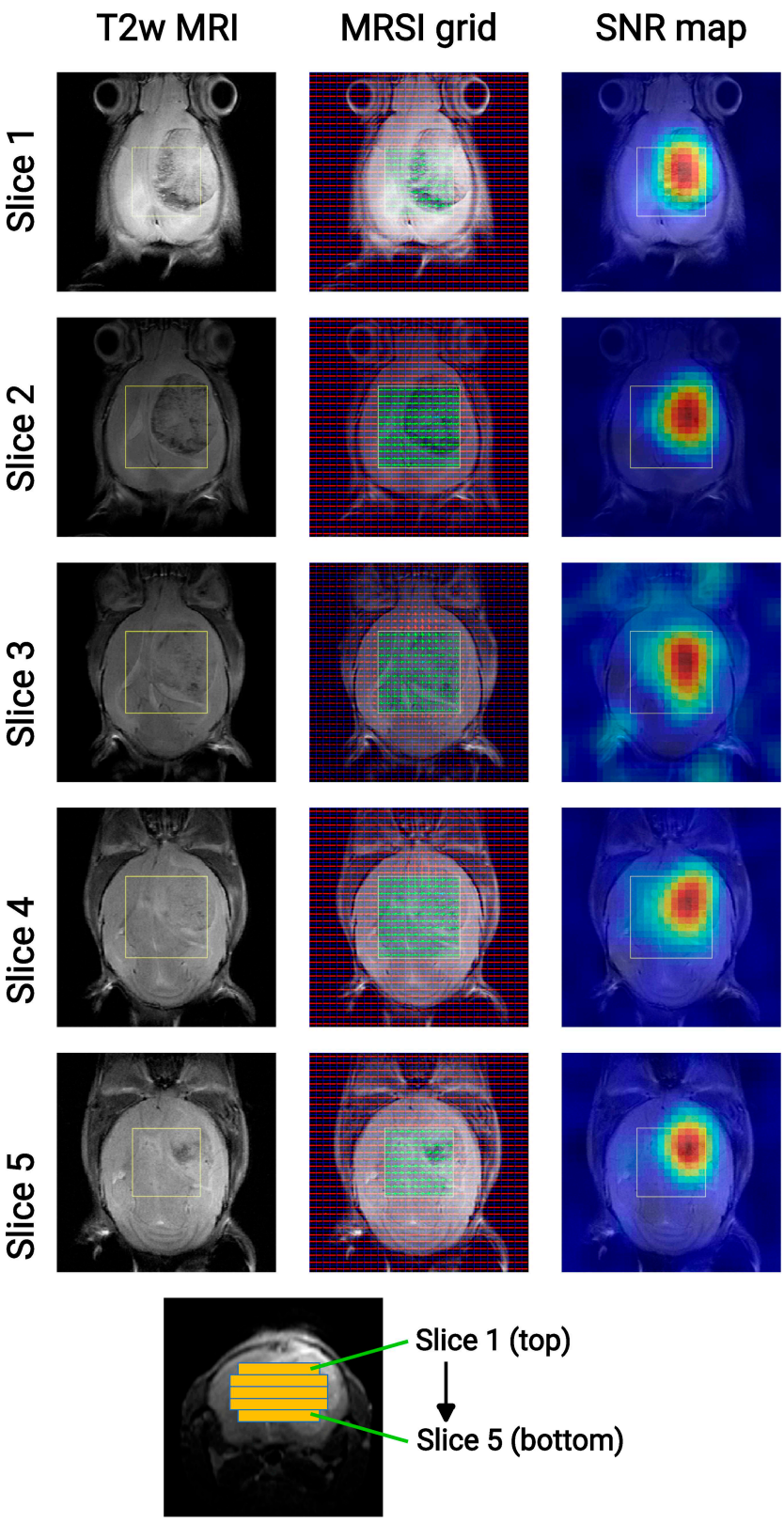

Figure 6. High-resolution MRSI-semiLASER grids in a GL261 tumor-bearing mouse. T2w coronal reference images (**left**) showing in yellow the localization of five contiguous 0.8 mm coronal grids prescribed across the mouse brain, covering the tumor and avoiding the scalp. Each MRSI grid was shimmed individually. The corresponding MRSI grids graphically superimposed to the T2w image are shown for each slice (**middle**). On the **right**, Lac/ML/MM mapsat ca. 1.3 ppm are overlaid on the corresponding T2w images, with the color scale representing SNR (blue, lower SNR; red, higher SNR). The bottom panel shows a T2w axial image illustrating the relative positioning of the five contiguous slices (slice 1 at the top to slice 5 at the bottom).

https://doi.org/10.3390/app16083788

4. Discussion

This study was designed to focus specifically on comparative sequence performance at the level of fundamental spectral characteristics of relevance for improving pattern recognition-based analysis [32–34]. Accordingly, the evaluation was restricted to direct spectral quality metrics, namely signal-to-noise ratio and full width at half maximum. Quantitative metabolite concentration estimates were not performed since the acquisition protocol and study design were not configured for this purpose.

4.1. Implementation of MRSI-semiLASER

The implementation of the MRSI-semiLASER on a Bruker Biospec 70/30 USR scanner equipped with the ParaVision 5.1 software afforded reproducible acquisition of the ^{1}H MR spectra, first in benchmarking in vitro tests and later for in vivo applications. The obtained spectral patterns were found to be equivalent to the CSI-PRESS spectra and, on several occasions, better resolved than the normal PRESS spectra. A consistent feature of the results was that MRSI-semiLASER provided a higher SNR as compared to CSI-PRESS. The SNR maps obtained using the MRSI-semiLASER for different metabolites such as NAA and Lac had more spatial distribution homogeneity than the maps from the CSI-PRESS sequence due to better excitation profile of the adiabatic refocusing pulses and the reduction in chemical shift displacement errors, affecting mainly the voxels at the edges of the VOI. Voxels closer to the edge of the VOI were mostly suitable for the evaluation in MRSI-semiLASER, whereas CSI-PRESS presented more low-quality voxels. In this study, bad-quality spectra were estimated at 8% and 18% for MRSI-semiLASER and CSI-PRESS, respectively, based on the predefined visual criteria, in line with [38], which demonstrated that employing a PRESS volume selection sequence at 3 T resulted in 17% of voxels exhibiting poor-quality spectra compared to 11% for semiLASER applied to 3 T ^{1}H MR spectroscopic imaging of the prostate [38,39]. It is worth mentioning that the metabolite choice is related to the relevance of such metabolites not only in representative patterns of normal and tumor spectra but also in classification studies, distinguishing tumor from normal tissue and non-responding from responding tumors, as highlighted in activation maps shown in [19].

MRS community consensus [23,40] has recommended the semiLASER localization sequence over PRESS for MRS studies. SemiLASER has been widely used in clinical studies mainly for SV MRS [30,41,42] but also for MRSI [43–45]. However, to the best of our knowledge, only two studies have reported using MRSI-semiLASER in preclinical studies. Miyasaka et al. [46] used a semiLASER sequence to demonstrate the feasibility of obtaining ^{1}H spectroscopic imaging on the mouse brain at 9.4 T and to assess regional differences in NAA/Cr ratios of the basal ganglia, hippocampus, thalamus, and cerebellum. A Hanning filter was applied in the spatial domain to the acquired data, as done in our study; however, no comparison to the PRESS-CSI performance was demonstrated. Moreover, Weiss et al. [47] have also implemented a semiLASER MRSI sequence and compared it with a standard PRESS CSI sequence at high magnetic field strength (17.6 T), with in vivo application on post-natal mouse brain metabolism. They reported that their implemented semiLASER MRSI, using weighted k-space averaging as well, provided high-quality spectra with a reduction in CSDE. However, the SNR values measured with semiLASER versus PRESS were not assessed. In this work, we have applied MRSI-semiLASER in mouse brain tumors for the first time, showing that our sequence implementation aligns with these previous findings, as well as a reduction in CSDEs and improved spectral profiles. Additionally, we have quantitatively compared the SNR as a main performance metric to demonstrate the differences between the implemented MRSI-semiLASER and our current standard CSI-PRESS protocol.

4.2. MRSI-semiLASER in Brain Tumors

Metabolic information was successfully obtained in GL261 tumor-bearing mice. Increased slice-direction spatial resolution was achieved using MRSI-semiLASER, which was able to acquire an extra slice within the same tumor volume. When decreasing the slice thickness from 1 mm to 0.8 mm, we expected to suffer a 20% reduction in the SNR based on volume differences; however, the SNR was maintained above the expected level. A possible explanation for this may be the fact that narrower water FWHM were obtained in spectra acquired at 0.8 mm, possibly indicating better B0 homogeneity in thinner slices, which resulted in narrower and more intense metabolite peaks and consequently higher SNR values since the SNR was measured as peak height over the standard deviation of the noise. Relative to our routine four-slice CSI-PRESS protocol, the five-slice MRSI-semiLASER protocol yielded an overall ~45% more usable and meaningful data (see Table S7), driven by both the extra slice and the lower proportion of poor-quality spectra per grid. This substantial increase may strengthen the downstream pattern recognition-based post-processing [18,20].

The aim of this study was to develop a reliable in vivo MRSI technique for advancing the non-invasive investigation of therapy response in a murine model of GL261 glioblastoma, with improved spatial homogeneity and spectral quality. In line with this technical focus, the analysis performed in tumor-bearing mice was intentionally kept descriptive. Our objective was to benchmark the intrinsic performance of MRSI-semiLASER relative to CSI-PRESS in terms of spectral quality, the SNR, and spatial definition rather than to conduct quantitative metabolic profiling. Moreover, our downstream studies rely on whole-spectrum pattern analysis rather than on absolute metabolite quantification, and such modeling falls outside the scope of this implementation-focused work. Future studies will need to evaluate whether our current classifier [27], trained exclusively with sources from spectra acquired using the Bruker stock CSI-PRESS sequence, is robust enough for MRSI-semiLASER datasets. If not, retraining the data from both CSI-PRESS and MRSI-semiLASER sequences may be necessary to improve the robustness of tumor mass evaluation when using the new MRSI-semiLASER acquisition method.

Although semiLASER offers clear advantages in terms of spectral homogeneity and the SNR, its use at 7 T also involves practical trade-offs that should be considered. The adiabatic refocusing pulses required for semiLASER lead to higher RF deposition, which can increase SAR and may constrain experimental flexibility when shorter TRs are desired. Although SAR could not be quantified on our preclinical system, continuous monitoring confirmed that animal core temperature remained stable within ±1 °C even during the longest acquisitions (~4 h), and no adverse physiological effects were observed. It should be emphasized that the absence of physiological instability does not substitute for a formal assessment of motion sensitivity or RF-related effects, which were beyond the scope of this study. In addition, semiLASER imposes a longer minimum TE than PRESS due to the duration of adiabatic pulses; while this does not strongly affect major singlet metabolites, it may influence the detection of compounds with short T2 or strong J-coupling. Nonetheless, in our preclinical settings, these constraints were manageable and did not outweigh the substantial gains in spectral quality and usable data yielded by semiLASER.

To date, the implemented sequence has been validated only in mouse brain tumor studies; however, it may have broader applicability to other metabolic brain disorder investigations, which warrants further investigation. The implemented MRSI-semiLASER sequence, along with the corresponding implementation instructions, has been made openly accessible through the Zenodo repository (https://zenodo.org/records/18461488 accessed on 7 February 2026). Notably, the performance of the semiLASER sequence can be influenced by factors such as the scanner's magnetic field strength, gradient strength,

and RF pulse characteristics. Therefore, it is important to check the individual system requirements to ensure optimal performance and data quality using the implemented sequence described here.

5. Limitations of the Study

This study has some limitations, which should be acknowledged. First, the in vivo sample size was small (n = 3 per group), reflecting the exploratory nature of the work and our adherence to 3R principles. Although the improvements in the SNR with MRSI-semiLASER were consistent and supported by paired statistical analyses and large within-subject effect sizes, the limited sample size reduces the statistical power and constrains the generalizability of our findings.

Second, the comparison between MRSI-semiLASER and CSI-PRESS was performed at their respective minimum echo times (TE = 27 ms vs. 14 ms), which reflects their optimal operational settings on our system. However, this difference limits the direct comparability of the two sequences, since TE influences signal evolution through T2 relaxation and J-coupling effects. Although major singlet metabolites such as NAA and creatine are less affected, macromolecules and mobile lipids may show greater TE dependence. The superior SNR observed with MRSI-semiLASER despite its longer TE supports the robustness of its adiabatic refocusing pulses, but the TE mismatch remains a methodological limitation. A fully TE-matched comparison would require a prospectively designed protocol including additional calibration and relaxation measurements beyond the scope of the present study.

Finally, the total in vivo acquisition time (~3.5 h) is relatively long. Although physiological stability was maintained throughout all experiments by continuous monitoring of breathing rate and body temperature, together with controlled anesthesia and a warm-water heating system, extended acquisition times may pose challenges in studies involving animals with large or advanced tumors. No signs of distress or instability were observed in the animals included in this study. However, the long scan duration also introduces a technical limitation: motion sensitivity and RF-related effects were not directly assessed. In particular, we did not perform a dedicated sequence-specific assessment of motion sensitivity or potential differential susceptibility to motion artifacts between MRSI-semiLASER and CSI-PRESS, nor did we evaluate the impact of the higher RF power deposition required for semiLASER on motion-related signal stability. While no motion-related degradation was visually detected in our datasets, a systematic comparison would require a prospectively designed protocol and should therefore be addressed in future work. Future implementations may also benefit from acceleration strategies for reducing the overall scan time.

Therefore, despite these limitations, the consistently improved SNR and spectral definition observed across phantom, wild-type, and tumor datasets support the technical robustness of the implemented MRSI-semiLASER sequence.

6. Conclusions

The MRSI-semiLASER sequence is a valuable tool for studying brain metabolic changes with promising potential in preclinical research. Successful implementation of the MRSI-semiLASER sequence, with a 1.1–1.3-fold improvement in the SNR in phantoms and in vivo mice compared to the stock Bruker CSI-PRESS sequence, has been duly verified and reported. Enhanced spatial resolution was achieved by reducing the slice thickness in GL261 tumor-bearing mice. Specifically, decreasing the slice thickness from 1 mm to 0.8 mm enabled the acquisition of a greater number of slices covering the tumor volume. While the improvement in slice-direction sampling may appear modest, its

incorporation into our multi-slice protocol yielded an overall ~45% increase in usable spectra. This substantially expanded dataset may facilitate pattern recognition analyses by providing richer spatial and spectral information, although no pattern recognition performance was evaluated in the present study. Overall, these technical improvements may be relevant for the design of future longitudinal studies aiming to maximize data yield per subject. The implemented MRSI-semiLASER sequence, validated for mouse brain tumor studies, has been deposited in the Zenodo repository, ensuring open access and long-term preservation.

Supplementary Materials: The following supporting information can be downloaded at: https://www.mdpi.com/article/10.3390/app16083788/s1, Figure S1: Schematic sequence diagram of the implemented MRSI-semiLASER sequence; Figure S2: In vitro repeatability (intraday) and reproducibility (interday) study; Figure S3: In vitro repeatability study; Figure S4: Metabolite SNR averages in phantom; Figure S5: In vivo spectra; Figure S6: Metabolite SNR averages in vivo; Table S1: Central and bottom-right sub-grids in phantom experiments—MRSI-semiLASER vs. CSI-PRESS; Table S2: MRSI-semiLASER vs. CSI-PRESS intra-day and interday mean SNR values; Table S3: Central and bottom-right sub-grids in vivo experiments in WT mouse MRSI-semiLASER vs. CSI-PRESS; Table S4: In vivo in WT mouse MRSI-semiLASER vs. CSI-PRESS mean SNR values; Table S5: In vivo tumor mouse MRSI-semiLASER vs. CSI-PRESS mean Lac/ML/MM SNR; Table S6: 0.8 mm vs. 1 mm slice SNR comparison for in vivo tumor-bearing mouse using MRSI-semiLASER; Table S7: Multi-slice MRSI-semiLASER vs. CSI-PRESS in vivo protocol comparison.

Author Contributions: Conceptualization, C.A., M.E.C., and S.L.-P.; methodology, Z.J., M.M.-A., G.V.M., M.E.C., and S.L.-P.; software, Z.J.; validation, M.E.C. and S.L.-P.; formal analysis, Z.J., M.E.C., and S.L.-P.; investigation, Z.J., M.E.C., and S.L.-P.; resources, A.P.C.; data curation, Z.J., M.E.C., and S.L.-P.; writing—original draft preparation, Z.J. and S.L.-P.; writing—review and editing, Z.J., G.V.M., A.P.C., C.A., M.E.C., and S.L.-P.; visualization, Z.J., M.E.C., and S.L.-P.; supervision, C.A., A.P.C., M.E.C., and S.L.-P.; project administration, C.A., M.E.C., and S.L.-P.; funding acquisition, C.A. and A.P.C. All authors have read and agreed to the published version of the manuscript.

Funding: This research was funded by European Commission, Marie Curie Initial Training Networks (ITN), H2020-MSCA-ITN-2018, proposal 813120 to C.A. It was also funded by Centro de Investigación Biomédica en Red—Bioingeniería, Biomateriales y Nanomedicina (CIBER-BBN [http://www.ciber-bbn.es/en, accessed on 15 September 2025], CB06/01/0010), an initiative of the Instituto de Salud Carlos III (Spain) co-funded by EU Fondo Europeo de Desarrollo Regional (FEDER). This project has received funding from the European Union's Horizon 2020 research and innovation programme under the Marie Skłodowska-Curie Actions, Grant Agreement No. 813120 (INSPiRE-MED). Z.J. was recipient of a Marie Skłodowska-Curie early-stage researcher fellowship of the INSPiRE-MED project. A.P.C. and C.A. received funding from the ATTRACT project funded by the EC under Grant Agreement 777222. A.P.C. was also funded by PID2023-147750NB-I00 funded by MCIN/AEI/10.13039/501100011033. We acknowledge the UAB Predoctoral training program (14ª Convocatoria PIF-19612, predoctoral fellowships for M.M-A.). A.P.C. and C.A. acknowledge 2021 XARDI 00021 (XarTEC SALUT) for support.

Institutional Review Board Statement: The animal study protocol was approved by the Institutional Review Board (Comitè d'Ètica en la Recerca CERec https://www.uab.cat/ca/etica-recerca accessed on 15 September 2025) of the Universitat Autònoma de Barcelona (protocol code CEEAH 3665/DMAH 9685 and date of approval 19 December 2017).

Informed Consent Statement: Not applicable.

Data Availability Statement: All magnetic resonance raw data files, the implemented MRSI-semiLASER sequence, along with the corresponding implementation instructions, are available from the Zenodo repository [https://zenodo.org/records/18461488 (accessed on 7 February 2026)].

https://doi.org/10.3390/app16083788

Acknowledgments: Time allocated at the joint nuclear magnetic resonance facility of the Universitat Autònoma de Barcelona and Centro de Investigación Biomédica en Red—Bioingeniería, Biomateriales y Nanomedicina (CIBER-BBN) (Cerdanyola del Vallès, Spain), Unit 25 of NANBIOSIS (https://www.nanbiosis.es/portfolio/u25-nmr-biomedical-application-i/ accessed on 15 September 2025) is gratefully acknowledged.

Conflicts of Interest: The authors declare no conflicts of interest.

Abbreviations

The following abbreviations are used in this manuscript:

^{1}H	proton
AFP	adiabatic full passage
Cho	choline
CoV	coefficient of variation
Cr	creatine
CSDE	chemical shift displacement error
CSI	chemical shift imaging
FOV	field of view
FWHM	full width at half maximum
HS	hyperbolic secant
Lac	lactate
ML	mobile lipids
MM	macromolecules + mobile lipids
MRI	magnetic resonance imaging
MRS	magnetic resonance spectroscopy
MRSI	magnetic resonance spectroscopic imaging
MTX	matrix size
NAA	N-acetylaspartate
NaN_3	sodium azide
FDR	false discovery rate
PRESS	point-resolved spectroscopy
RARE	rapid acquisition with relaxation enhancement
RC	repeatability coefficient
semiLASER	semi-localized adiabatic selective refocusing
SD	standard deviation
SNR	signal-to-noise ratio
SI	supporting information
T2w	T2-weighted imaging
TAT	total acquisition time
TE	echo time
TR	repetition time
VOI	volume of interest
WT	wild-type

References

1. Skoch, A.; Jiru, F.; Bunke, J. Spectroscopic imaging: Basic principles. *Eur. J. Radiol.* **2008**, *67*, 230–239.
2. Van Der Graaf, M. In vivo magnetic resonance spectroscopy: Basic methodology and clinical applications. *Eur. Biophys. J.* **2010**, *39*, 527–540.
3. Lee, P.; Adany, P.; Choi, I.Y. Imaging based magnetic resonance spectroscopy (MRS) localization for quantitative neurochemical analysis and cerebral metabolism studies. *Anal. Biochem.* **2017**, *529*, 40.
4. Bogner, W.; Otazo, R.; Henning, A. Accelerated MR spectroscopic imaging—A review of current and emerging techniques. *NMR Biomed.* **2021**, *34*, e4314.
5. Weinberg, B.D.; Kuruva, M.; Shim, H.; Mullins, M.E. Clinical Applications of Magnetic Resonance Spectroscopy in Brain Tumors: From Diagnosis to Treatment. *Radiol. Clin. North Am.* **2021**, *59*, 349–362.

6. Delgado-Goni, T.; Ortega-Martorell, S.; Ciezka, M.; Olier, I.; Candiota, A.P.; Julià-Sapé, M.; Fernández, F.; Pumarola, M.; Lisboa, P.J.; Arús, C. MRSI-based molecular imaging of therapy response to temozolomide in preclinical glioblastoma using source analysis. *NMR Biomed.* **2016**, *29*, 732–743.
7. Arlauckas, S.P.; Browning, E.A.; Poptani, H.; Delikatny, E.J. Imaging of cancer lipid metabolism in response to therapy. *NMR Biomed.* **2019**, *32*, e4070.
8. Bhaduri, S.; Kelly, C.L.; Lesbats, C.; Sharkey, J.; Ressel, L.; Mukherjee, S.; Platt, M.D.; Delikatny, E.J.; Poptani, H. Metabolic changes in glioblastomas in response to choline kinase inhibition: In vivo MRS in rodent models. *NMR Biomed.* **2023**, *36*, e4855.
9. Lin, A.; Andronesi, O.; Bogner, W.; Choi, I.; Coello, E.; Cudalbu, C.; Juchem, C.; Kemp, G.J.; Kreis, R.; Krššák, M.; et al. Minimum Reporting Standards for in vivo Magnetic Resonance Spectroscopy (MRSinMRS): Experts' consensus recommendations. *NMR Biomed.* **2021**, *34*, e4484.
10. Horská, A.; Berrington, A.; Barker, P.B.; Tkáč, I. Magnetic Resonance Spectroscopy: Clinical Applications. In *Functional Neuroradiology: Principles and Clinical Applications*, 2nd Ed.; Springer: Cham, Switzerland, 2023; pp. 241–292. https://doi.org/10.1007/978-3-031-10909-6_10.
11. Simões, R.V.; Delgado-Goñi, T.; Lope-Piedrafita, S.; Arús, C. 1H-MRSI pattern perturbation in a mouse glioma: The effects of acute hyperglycemia and moderate hypothermia. *NMR Biomed.* **2010**, *23*, 23–33.
12. Delgado-Goñi, T.; Martín-Sitjar, J.; Simões, R.V.; Acosta, M.; Lope-Piedrafita, S.; Arús, C. Dimethyl sulfoxide (DMSO) as a potential contrast agent for brain tumors. *NMR Biomed.* **2013**, *26*, 173–184.
13. Saito, S.; Ueda, J. Preclinical magnetic resonance imaging and spectroscopy in the fields of radiological technology, medical physics, and radiology. *Radiol. Phys. Technol.* **2024**, *17*, 47–59.
14. Szatmári, T.; Lumniczky, K.; Désaknai, S.; Trajcevski, S.; Hídvégi, E.J.; Hamada, H.; Sáfrány, G. Detailed characterization of the mouse glioma 261 tumor model for experimental glioblastoma therapy. *Cancer Sci.* **2006**, *97*, 546–553.
15. Renner, D.N.; Malo, C.S.; Jin, F.; Parney, I.F.; Pavelko, K.D.; Johnson, A.J. Improved Treatment Efficacy of Antiangiogenic Therapy when Combined with Picornavirus Vaccination in the GL261 Glioma Model. *Neurotherapeutics* **2016**, *13*, 226–236.
16. Reardon, D.A.; Gokhale, P.C.; Klein, S.R.; Ligon, K.L.; Rodig, S.J.; Ramkissoon, S.H.; Jones, K.L.; Conway, A.S.; Liao, X.; Zhou, J.; et al. Glioblastoma eradication following immune checkpoint blockade in an orthotopic, immunocompetent model. *Cancer Immunol. Res.* **2016**, *4*, 124–135.
17. Tritz, Z.P.; Ayasoufi, K.; Johnson, A.J. Anti-PD-1 checkpoint blockade monotherapy in the orthotopic GL261 glioma model: The devil is in the detail. *Neurooncol. Adv.* **2021**, *3*, vdab066.
18. Arias-Ramos, N.; Ferrer-Font, L.; Lope-Piedrafita, S.; Mocioiu, V.; Julià-Sapé, M.; Pumarola, M.; Arús, C.; Candiota, A.P. Metabolomics of therapy response in preclinical glioblastoma: A multi-slice MRSI-based volumetric analysis for noninvasive assessment of temozolomide treatment. *Metabolites* **2017**, *7*, 20.
19. Ortega-Martorell, S.; Olier, I.; Hernandez, O.; Restrepo-Galvis, P.D.; Bellfield, R.A.A.; Candiota, A.P. Tracking Therapy Response in Glioblastoma Using 1D Convolutional Neural Networks. *Cancers* **2023**, *15*, 4002.
20. Wu, S.; Calero-Pérez, P.; Arús, C.; Candiota, A.P. Anti-pd-1 immunotherapy in preclinical gl261 glioblastoma: Influence of therapeutic parameters and non-invasive response biomarker assessment with mrsi-based approaches. *Int. J. Mol. Sci.* **2020**, *21*, 8775.
21. Calero-Pérez, P.; Wu, S.; Arús, C.; Candiota, A.P. Immune system-related changes in preclinical GL261 glioblastoma under TMZ treatment: Explaining MRSI-based nosological imaging findings with RT-PCR analyses. *Cancers* **2021**, *13*, 2663.
22. Scheenen, T.W.J.; Klomp, D.W.J.; Wijnen, J.P.; Heerschap, A. Short echo time 1H-MRSI of the human brain at 3T with minimal chemical shift displacement errors using adiabatic refocusing pulses. *Magn. Reson. Med.* **2008**, *59*, 1–6.
23. Öz, G.; Deelchand, D.K.; Wijnen, J.P.; Mlynárik, V.; Xin, L.; Mekle, R.; Wilson, M. Advanced single voxel 1H magnetic resonance spectroscopy techniques in humans: Experts' consensus recommendations. *NMR Biomed.* **2021**, *34*, e4236.
24. Jalnefjord, O.; Pettersson, P.; Lundholm, L.; Ljungberg, M. Simulated basis sets for semi-LASER: The impact of including shaped RF pulses and magnetic field gradients. *Magn. Reson. Mater. Phys. Biol. Med.* **2021**, *34*, 545–554.
25. Jona, G.; Furman-Haran, E.; Schmidt, R. Realistic head-shaped phantom with brain-mimicking metabolites for 7 T spectroscopy and spectroscopic imaging. *NMR Biomed.* **2021**, *34*, e4421.
26. Garofalo, S.; Porzia, A.; Mainiero, F.; Di Angelantonio, S.; Cortese, B.; Basilico, B.; Pagani, F.; Cignitti, G.; Chece, G.; Maggio, R.; et al. Environmental stimuli shape microglial plasticity in glioma. *Elife* **2017**, *6*, e33415.
27. Wu, S.; Calero-Pérez, P.; Villamañan, L.; Arias-Ramos, N.; Pumarola, M.; Ortega-Martorell, S.; Julià-Sapé, M.; Arús, C.; Candiota, A.P. Anti-tumour immune response in GL261 glioblastoma generated by Temozolamide Immune-Enhancing Metronomic Schedule monitored with MRSI-based nosological images. *NMR Biomed.* **2020**, *33*, e4229.

28. von Kienlin, M.; Ziegler, A.; Le Fur, Y.; Rubin, C.; Décorps, M.; Rémy, C. 2D-spatial/2D-spectral spectroscopic imaging of intracerebral gliomas in rat brain. *Magn. Reson. Med.* **2000**, *43*, 211–219.
29. Gruetter, R. Automatic, localized in Vivo adjustment of all first-and second-order shim coils. *Magn. Reson. Med.* **1993**, *29*, 804–811.
30. Landheer, K.; Gajdošík, M.; Juchem, C. A semi-LASER, single-voxel spectroscopic sequence with a minimal echo time of 20.1 ms in the human brain at 3 T. *NMR Biomed.* **2020**, *33*, e4324.
31. Javed, Z. Implementation of High-Resolution MRSI Methods in a Pre-Clinical Scanner, and Optimization for Brain Longitudinal Studies of Therapy Response in Mice Glioma Models. Doctoral Thesis, Universitat Autònoma de Barcelona, Cerdanyola del Vallès, Spain, 2023. https://doi.org/10803/690988.
32. Craven, A.R.; Bell, T.K.; Ersland, L.; Harris, A.D.; Hugdahl, K.; Oeltzschner, G. Linewidth-related bias in modelled concentration estimates from GABA-edited 1H-MRS. *bioRxiv* **2024**, bioRxiv:2024.02.27.582249. https://doi.org/10.1101/2024.02.27.582249.
33. Vella, O.; Bagshaw, A.P.; Wilson, M. SLIPMAT: A pipeline for extracting tissue-specific spectral profiles from 1H MR spectroscopic imaging data. *Neuroimage* **2023**, *277*, 120235.
34. Zhang, Y.; Shen, J. Effects of noise and linewidth on in vivo analysis of glutamate at 3 Tesla. *J. Magn. Reson.* **2020**, *314*, 106732.
35. Simpson, R.; Devenyi, G.A.; Jezzard, P.; Hennessy, T.J.; Near, J. Advanced processing and simulation of MRS data using the FID appliance (FID-A)—An open source, MATLAB-based toolkit. *Magn. Reson. Med.* **2017**, *77*, 23–33.
36. Carstensen, B. Comparing Clinical Measurement Methods: A Practical Guide. In *Comparing Clinical Measurement Methods: A Practical Guide*; Wiley: Hoboken, NJ, USA, 2010; pp. 1–160. https://doi.org/10.1002/9780470683019.
37. Cudalbu, C.; Cavassila, S.; Ratiney, H.; Beuf, O.; Briguet, A.; Graveron-Demilly, D. Metabolite concentrations of healthy mouse brain by Magnetic Resonance spectroscopy at 7 Tesla. In Proceedings of the 27th Annual International Conference of the IEEE Engineering in Medicine and Biology Society, Shanghai, China, 1–4 September 2005; Volume 7, pp. 1392–1395.
38. Wright, A.J.; Kobus, T.; Selnæs, K.M.; Gribbestad, I.S.; Weiland, E.; Scheenen, T.W.J.; Heerschap, A. Quality control of prostate 1H MRSI data. *NMR Biomed.* **2013**, *26*, 193–203.
39. Stamatelatou, A.; Scheenen, T.W.J.; Heerschap, A. Developments in proton MR spectroscopic imaging of prostate cancer. *Magn. Reson. Mater. Phys. Biol. Med.* **2022**, *35*, 645–665.
40. Wilson, M.; Andronesi, O.; Barker, P.B.; Bartha, R.; Bizzi, A.; Bolan, P.J.; Brindle, K.M.; Choi, I.-Y.; Cudalbu, C.; Dydak, U.; et al. Methodological consensus on clinical proton MRS of the brain: Review and recommendations. *Magn. Reson. Med.* **2019**, *82*, 527–550.
41. Penner, J.; Bartha, R. Semi-LASER 1H MR spectroscopy at 7 Tesla in human brain: Metabolite quantification incorporating subject-specific macromolecule removal. *Magn. Reson. Med.* **2015**, *74*, 4–12.
42. Deelchand, D.K.; Berrington, A.; Noeske, R.; Joers, J.M.; Arani, A.; Gillen, J.; Schär, M.; Nielsen, J.; Peltier, S.; Seraji-Bozorgzad, N.; et al. Across-vendor standardization of semi-LASER for single-voxel MRS at 3T. *NMR Biomed.* **2021**, *34*, e4218.
43. Kumaragamage, C.; Coppoli, A.; Brown, P.B.; McIntyre, S.; Nixon, T.W.; De Feyter, H.M.; Mason, G.F.; de Graaf, R.A. Short symmetric and highly selective asymmetric first and second order gradient modulated offset independent adiabaticity (GOIA) pulses for applications in clinical MRS and MRSI. *J. Magn. Reson.* **2022**, *341*, 107247.
44. Gholizadeh, N.; Greer, P.B.; Simpson, J.; Goodwin, J.; Fu, C.; Lau, P.; Siddique, S.; Heerschap, A.; Ramadan, S. Diagnosis of transition zone prostate cancer by multiparametric MRI: Added value of MR spectroscopic imaging with sLASER volume selection. *J. Biomed. Sci.* **2021**, *28*, 54.
45. Steinseifer, I.K.; Philips, B.W.; Gagoski, B.; Weiland, E.; Scheenen, T.W.J.; Heerschap, A. Flexible proton 3D MR spectroscopic imaging of the prostate with low-power adiabatic pulses for volume selection and spiral readout. *Magn. Reson. Med.* **2017**, *77*, 928–935.
46. Miyasaka, N.; Takahashi, K.; Hetherington, H.P. 1H MMR spectroscopic imaging of the mouse brain at 9.4 T. *J. Magn. Reson. Imaging* **2006**, *24*, 908–913.
47. Weiss, K.; Melkus, G.; Jakob, P.M.; Faber, C. Quantitative in vivo 1H spectroscopic imaging of metabolites in the early postnatal mouse brain at 17.6 T. *Magn. Reson. Mater. Phys. Biol. Med.* **2009**, *22*, 53–62.